Boundary Fitting Based Segmentation of Fluorescence Microscopy Images

Soonam Lee[a], Paul Salama[b], Kenneth W. Dunn[c] and Edward J. Delp[a]

[a]*Video and Image Processing Laboratory (VIPER)*
School of Electrical and Computer Engineering
Purdue University, West Lafayette, Indiana 47907, USA
[b]*Department of Electrical and Computer Engineering*
Indiana University, Indianapolis, Indiana 46202, USA
[c]*Division of Nephrology*
School of Medicine
Indiana University, Indianapolis, Indiana 46202, USA

ABSTRACT

Segmentation is a fundamental step in quantifying characteristics, such as volume, shape, and orientation of cells and/or tissue. However, quantification of these characteristics still poses a challenge due to the unique properties of microscopy volumes. This paper proposes a 2D segmentation method that utilizes a combination of adaptive and global thresholding, potentials, z direction refinement, branch pruning, end point matching, and boundary fitting methods to delineate tubular objects in microscopy volumes. Experimental results demonstrate that the proposed method achieves better performance than an active contours based scheme.

Keywords: image segmentation, adaptive thresholding, ellipse fitting, biomedical imaging

1. INTRODUCTION

Advances in fluorescence microscopy have enabled biologists to image deeper into tissue than previously achievable [1], [2], [3]. Of increasing interest is the application of quantitative analysis to acquired 3D image stacks. However, the volume of data makes manual quantification, especially of each cell or tissue, tedious and error-prone. Thus, automated processing methods, especially image segmentation, become vital.

Segmentation of fluorescence microscopy images remains challenging due to the loss in contrast and resolution by the significant scattering of light in biological tissue. For this reason, segmentation approaches that are successful at distinguishing objects at the surface of tissue samples increasingly fail at depth. In addition, boundaries of biological objects, which tend to be non rigid and tend to vary in shape and orientation, are not always clearly and completely delineated by fluorescent probes. Moreover, the resolution along the z axis is approximately 4 times less than along the x and y directions [4], [5].

There have been efforts to develop automatic segmentation methods for biomedical image data sets that attempt to address these issues, that in general have relied on thresholding, the watershed algorithm [6], and active contours [7]. Thresholding based methods are typically limited in their performance when the objects to be segmented are not well-defined. Thus, thresholding is normally used in conjunction with other methods such as gradient flow tracking [8] or the watershed technique [9]. Similarly, the watershed scheme is combined with region splitting and merging method [10], since it tends to generate larger segmented regions than desired.

Alternatively, active contour methods [7] recursively deform an initial contour to fit a desired object based on the minimization of an energy functional. However, the performance of active contour methods rely on the initial contours chosen and can generate inaccurate segmentations. A method for addressing this issue suited for microscopy data that uses the Poisson inverse gradient was proposed in [11]. To circumvent the dependence of the

This work was supported by a George M. O'Brien Award from the National Institutes of Health NIH/NIDDK P50 DK 61594.

Imaging and Multimedia Analytics in a Web and Mobile World 2015, edited by Qian Lin, Jan P. Allebach, Zhigang Fan, Proc. of SPIE-IS&T Electronic Imaging, Vol. 9408, 940805
© 2015 SPIE-IS&T · CCC code: 0277-786X/15/$18 · doi: 10.1117/12.2085417

Downloaded From: http://proceedings.spiedigitallibrary.org/ on 02/16/2017 Terms of Use: http://spiedigitallibrary.org/ss/termsofuse.aspx

final outcome on the initial contour, [12] proposed integrating a background removal model with a region-based active contour method that uses multiple contour initializations to perform segmentation. Alternatively [13] proposed the use of random seed region-based active contours combined with multi-resolution, multi-scale, and region-growing to achieve multidimensional segmentation. Furthermore, [14] proposed the use of active surfaces, a 3D version of region-based active contours [7].

As indicated above, segmenting objects in biological images remains a challenging problem. This is further compounded by the fact that these objects can change shape and orientation with depth. An example of this are tubules, hollow biological tissues having tubular shape, that can be challenging for energy minimization based techniques to delineate [15]. There has however been recent work focused on segmenting tubules from biomedical images. In particular, [16], [17] proposed a minimal path based segmentation scheme that uses fast marching techniques. Also [18] described a scheme using geodesic active contours to detect tubular structures, and [15] used a combination of level set methods and the geodesic distance transform to segment multiple tubules.

In this paper, we describe a technique that segments 2D cross-sections of tubules in microscopy images using a combination of adaptive and global thresholding, potentials, z direction refinement, branch pruning, end point matching, and curve fitting. The aim here is to be able to segment the 2D cross-sections at various depths as an initial step to 3D segmentation of these objects. The performance of the proposed technique is compared to that of an active contours based method [7].

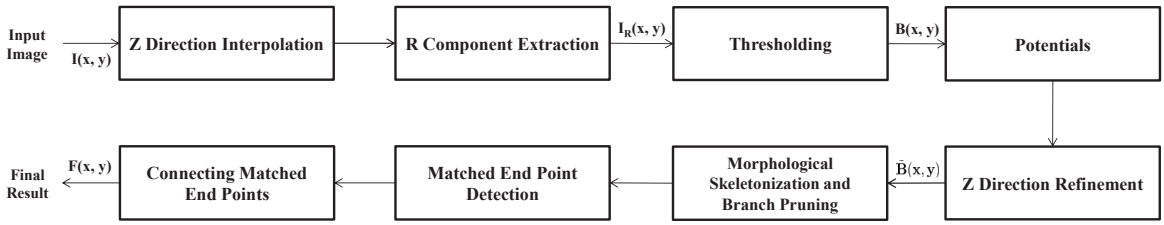

Figure 1. Block diagram of the proposed segmentation technique.

2. PROPOSED SCHEME

As mentioned above the objective of this work is to segment tubular structures present in microscopy images. Figure 1 highlights the various stages of the proposed technique. Representative images from two of the data sets being processed are provided in Figures 4a and 4g. Figure 4a shows an image from a 3D volume of rat kidney labeled with Hoechst 33342 (blue) and fluorescent phalloidin (red) dyes, whereas Figure 4g presents an image from a 3D volume of rat kidney labeled with Hoechst 33342 (blue) and a fluorescent lectin (red) dye. Both data sets were imaged using multiphoton fluorescence excitation microscopy [1], and in both cases the structures of interest reside mostly in the red (R) component of the data. Thus, as shown in Figure 1, the R component of each image is initially extracted. This is preceded however by an interpolation step where we use cubic interpolation to compensate for the fact that the resolution along the z direction is smaller than along the x and y direction.

Figures 4b and 4h depict the R components of the images shown in Figures 4a and 4g, respectively. As can be expected and observed both images have non-homogeneous intensities. Due to this non-homogeneity, we first utilize an adaptive thresholding scheme [19] that obtains local thresholds $T(x, y)$ at each location (x, y) based on a local neighborhood W centered at (x, y):

$$T(x, y) = m(x, y) \cdot \left[1 + k \cdot \left(\frac{s(x, y)}{R} - 1\right)\right], \tag{1}$$

where $m(x, y)$ and $s(x, y)$ are the empirical mean and variance of the pixel values within region W respectively, k a tuning parameter, and R the dynamic range of $s(x, y)$. The values of W, R, and k used in this paper are different from those proposed in [19] and will be provided in Section 3.

Downloaded From: http://proceedings.spiedigitallibrary.org/ on 02/16/2017 Terms of Use: http://spiedigitallibrary.org/ss/termsofuse.aspx

Due to the fluctuations in pixel intensities, adaptive thresholding produces false contours. To address this problem, we modify $T(x, y)$ using a global threshold T_G to produce a final threshold $T'(x, y)$ defined as:

$$T'(x, y) = max(T(x, y), T_G). \tag{2}$$

The value of T_G that effectively reduced the number of false contours, especially in dark regions, was empirically determined. Applying $T'(x, y)$ to each red channel $I_R(x, y)$ produced a corresponding binary image $B(x, y)$:

$$B(x, y) = \begin{cases} 1 & \text{if } I_R(x, y) > T'(x, y) \\ 0 & \text{if } I_R(x, y) \leq T'(x, y) \end{cases} . \tag{3}$$

We also investigated using edge detection methods such as the Canny operator [20] to detect object boundaries. Due to the nature of the data, the Canny operator did not produce results as well as the modified adaptive thresholding method used here.

$B(x, y)$ generally highlights object boundaries as well as lumen that appear as edges interior to an object, as shown in Figures 4c and 4i, respectively. The objective is to retain the object boundaries only. This is achieved by using potential functions and z direction refinement. We employ two different potential functions: potential for position (P_P) and potential for occupancy (P_O), weighted by two coefficients λ_1 and λ_2, respectively, to create total potential $P_T = \lambda_1 P_P + \lambda_2 P_O$. This will be utilized to separate foreground and background regions. The description of each potential function follows:

1. Potential for position, P_P.
   Since $B(x, y)$ contains unwanted edges, suppressing them should be necessary step. To do this, we first stack all the binary images $B(x, y)$ along the z direction to form a binary volume ($V(x, y, z)$). P_P is then obtained by convolving the binary volume with a 3D Gaussian filter $h(x, y, z)$:

   $$P_P(x, y, z) = V(x, y, z) * h(x, y, z). \tag{4}$$

   The Gaussian filter used here is $h(x, y, z) = \frac{1}{\sqrt{(2\pi)^3}} \exp\left(-\frac{x^2+y^2+z^2}{2}\right)$ and $*$ represents $3D$ convolution. Since $V(x, y, z)$ is binary, the value of P_P at each voxel is always between 0 and 1.

2. Potential for occupancy, P_O.
   Since $B(x, y)$ highlights both objects and lumens, P_O is designed such that pixels on the outer boundaries are assigned larger values and small values given to interior lumens. This is achieved by first labeling $B(x, y)$ using 2D connected components with an 8-neighborhood. In this case a connected component with an 8-neighborhood is a set of pixels connected horizontally, vertically, or diagonally, that have the same characteristics or features such as belonging to the same edge. To distinguish the different connected components, each component is assigned an unique label. Starting from an unlabeled non-zero pixel in $B(x, y)$, we assign the same label to all pixels that are connected to it within its 8-neighborhood. In addition, the neighbors of all the labeled current pixel's neighbors are given the same label and the process repeated until all the connected neighbors have been identified. This is now considered a connected component identified by a unique label. Once a single connected component has been identified, we locate the next non-zero unlabeled pixel in raster scan order and assign a different label to all the pixels in its associated neighborhood. The process of identifying and labeling another connected component is then repeated. This is continued until all the non-zero pixels in $B(x, y)$ have been labeled. At this stage all the pixels in $B(x, y)$ have been grouped into separate connected components that are identified by their unique labels. In addition, the size (s_{CC}) of each connected component, which is defined to be the number of pixels that constitute the connected component, as well as the locations of all the constituent pixels are recorded. Moreover, the smallest bounding rectangle containing all the pixels of each connected component is constructed for each connected component. The fraction, S, of how much each bounding rectangle is occupied by its corresponding connected component's pixels, defined as

   $$S \triangleq \frac{s_{CC}}{s_{BB}}, \tag{5}$$

Downloaded From: http://proceedings.spiedigitallibrary.org/ on 02/16/2017 Terms of Use: http://spiedigitallibrary.org/ss/termsofuse.aspx

where s_{BB} denotes the area of the bounding rectangle. The ratio S for each labeled connected component is otained and normalized such that the smallest S from $B(x, y)$ maps to 0 and the largest S maps to 1. We assign P_O to have a large value when S is small and vice-versa so that the potential P_O has relatively larger value at pixels on tubule boundaries than pixels interior to the object. Thus, we define P_O to be $P_O(x, y, z) = 1 - S$ at each x, y and z corresponding to the connected component's location.

3. Total potential, P_T.
   Once we obtain P_P and P_O, total potential (P_T) is obtained for each voxel location using

$$P_T(x, y, z) = \lambda_1 P_P(x, y, z) + \lambda_2 P_O(x, y, z), \tag{6}$$

   where λ_1 and λ_2 are non-negative weights such that $\lambda_1 + \lambda_2 = 1$. The value of weights λ_1, λ_2 are empirically determined to be 0.25 and 0.75 respectively. The value of P_T is thresholded using a threshold T_P to produce a thresholded total potential $\tilde{P}_T$ where

$$\tilde{P}_T(x, y, z) = \begin{cases} 1 & \text{if } P_T(x, y, z) > T_P \\ 0 & \text{if } P_T(x, y, z) \leq T_P \end{cases} . \tag{7}$$

   If $\tilde{P}_T = 1$ the corresponding voxel is considered to be part of an object/tubule boundary. If however, $\tilde{P}_T = 0$ then the voxel is deemed to be belonging to lumen. This combination of two potentials successfully removes most of the lumen and retains boundary.

To further refine $\tilde{P}_T$, we employ z direction information. Object/tubules boundaries are generally continuous and consistent along the z direction whereas lumen are not. We thus use a 1D Gaussian filter ($\psi(z)$) to convolve $\tilde{P}_T$ along the z direction:

$$P_F(x, y, z) = \tilde{P}_T(x, y, z) * \psi(z), \tag{8}$$

where $\psi(z) = \frac{1}{\sqrt{2\pi\sigma_z^2}} \exp\left(-\frac{z^2}{2\sigma_z^2}\right)$. P_F is then thresholded using threshold T_P to produce binary data. The image obtained after applying the potentials and z direction refinement is denoted by $\tilde{B}(x, y)$. The parameter values that we use for the potentials and z direction refinement are provided in Section 3.

While the previous procedure removes interior edges, yet as seen from Figures 4d and 4j not all resulting boundaries are fully connected and many have random protruding branches that are pruned through the following procedure:

1. Create a morphological skeleton. In this case we define a morphological skeleton to be the outcome of performing morphological thinning on $\tilde{B}(x, y)$. In particular, morphological thinning is achieved by iteratively performing morphological erosion using a 2×2 square structuring element to achieve a single-pixel-width skeleton [21].

2. Identify end points and branch points along each boundary. An end point is a point that has one or fewer neighbors in the morphological skeleton. A branch point is defined as a point that has 3 or more neighbors in the morphological skeleton. Record the number of end points before branch pruning and denote it as E_p^{i-1} where i is the number of branch pruning iterations.

3. Trace back a maximum of 7 edge pixels from each end point. While tracing back, obtain the locations of the pixels on the traversed path and check whether they are branch points.

4. For each end point, retain all pixels on the back path if there are no branch points. However, if there is a branch point among the pixels on the back path, then remove all pixels connecting the end point to the branch point but keep the branch point.

5. Repeat for all end points and count the number of end points after branch pruning. Denote it as E_p^i.

Downloaded From: http://proceedings.spiedigitallibrary.org/ on 02/16/2017 Terms of Use: http://spiedigitallibrary.org/ss/termsofuse.aspx

6. Perform branch pruning steps $(2-5)$ iteratively until a stopping criterion is met. This criterion is based on the relative change in number of end points at each iteration. In particular, define Q as

$$Q \triangleq \frac{|E_p^{i-1} - E_p^i|}{E_p^{i-1}}.$$

The iterative branch pruning is terminated when Q falls below 0.1.

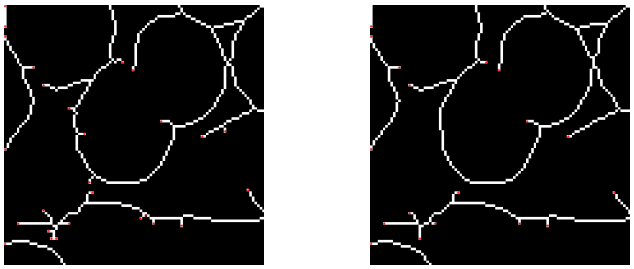

(a) Before pruning small branches (b) After pruning small branches

Figure 2. Example of pruning small branches from a morphological skeleton.

Figure 2 shows the outcome of applying the above procedure to the image in Figure 4d. As observed, small branches are successfully removed.

The next step is to reconnect the entire boundary. This is accomplished as follows:

1. Identify all end points. This is done as described above.
2. Obtain the Euclidean distance between all pairs of end points. If two end points are closer than a certain threshold τ_D, they are considered to be points on a common boundary and need to be connected to close the boundary. Such points are denoted as matching end points. In this paper, $\tau_D = 35$.
3. Having found all pairs of matching end points, obtain the "shortest path", based on geodesic distance [22], between any two matching end points while traversing that part of the boundary that already joins them. Figure 3 depicts two examples of shortest paths between two end points. In the figure, the matching end points are marked in red and the corresponding "shortest paths," based on geodesic distance, are highlighted in green.

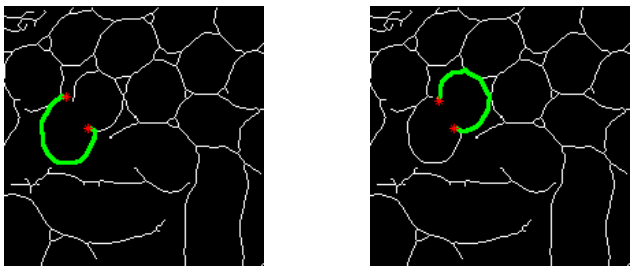

(a) (b)

Figure 3. Two "shortest paths" between two matching end points. The end points are indicated in red and the "shortest paths" in green.

4. Find an ellipse that best (in the least square sense) fits the shortest path between the two matching end points, while passing through the end points. This is formulated as a constrained least squares curve fitting problem. In particular, using the general form for conic sections

$$a\mathbf{x} \circ \mathbf{x} + 2b\mathbf{x} \circ \mathbf{y} + c\mathbf{y} \circ \mathbf{y} + 2d\mathbf{x} + 2f\mathbf{y} + g = 0, \tag{9}$$

Downloaded From: http://proceedings.spiedigitallibrary.org/ on 02/16/2017 Terms of Use: http://spiedigitallibrary.org/ss/termsofuse.aspx

where $\mathbf{x}$ and $\mathbf{y}$ are column vectors representing the x and y values of each pixel location on the shortest path and $\circ$ represents Hadamard product. Dividing both sides by a and re-arranging, we obtain $M\mathbf{p} = \mathbf{q}$, where $M = \begin{bmatrix}2\mathbf{x}\circ\mathbf{y} & \mathbf{y}\circ\mathbf{y} & 2\mathbf{x} & 2\mathbf{y} & \mathbf{1}\end{bmatrix}$, $\mathbf{p} = \begin{bmatrix}b/a & c/a & d/a & f/a & g/a\end{bmatrix}^T$, and $\mathbf{q} = -\mathbf{x}\circ\mathbf{x}$. Note that $\mathbf{1}$ is a vector whose entries are all 1. In addition, to ensure this formulation will form an ellipse we impose $b^2 - 4ac = -1$ as in [23] rather than imposing the general constraint $b^2 - 4ac < 0$. This leads to an overdetermined system if all the points lying on the shortest path between the matching end points are taken into account. Thus, to solve for the unknown coefficients in $\mathbf{p}$, we find $\mathbf{p}$ that minimizes the squared error $\frac{1}{2}\|M\mathbf{p} - \mathbf{q}\|_2^2$, while ensuring that the ellipse passes through the end points. Thus, we pose this as follows:

$$\min_{\mathbf{p}} \quad \tfrac{1}{2}\|M\mathbf{p} - \mathbf{q}\|_2^2 \tag{10}$$

$$\text{subject to} \quad G\mathbf{p} = \mathbf{h} \tag{11}$$

$$b^2 - 4ac = -1, \tag{12}$$

$$\text{where} \quad G = \begin{bmatrix}2x_{e_0}y_{e_0} & y_{e_0}^2 & 2x_{e_0} & 2y_{e_0} & 1\\ 2x_{e_1}y_{e_1} & y_{e_1}^2 & 2x_{e_1} & 2y_{e_1} & 1\end{bmatrix}$$

$$\mathbf{h} = \begin{bmatrix}-x_{e_0}^2 & -x_{e_1}^2\end{bmatrix}^T.$$

Here (x_{e_0}, y_{e_0}), (x_{e_1}, y_{e_1}) are the locations of the two matching end points, e_0 and e_1, respectively. Once the coefficients have been found they are used to join the matching end points using an elliptical curve.

After having completed the above procedures, there remain some exceptions. They are:

1. The solution to the constrained optimization problem does not result in an ellipse, or
2. The elliptical arc between two matching end points extends beyond the image boundary, or
3. The elliptical arc between two matching end points interferes with boundaries already identified.

In these three cases, the matched end points are left unconnected.

In addition, there are some end points that do not belong to the same connected component, yet are within a distance τ_D of each other. Such points are joined by a straight line unless the line intersects another already existing boundary. In the case of the latter, the points are left unconnected. Finally, a search is carried out for all remaining unconnected end points. These are connected to the closest object boundary via a straight line if the distance between the unconnected end points and closest object boundary is within $\tau_D/2$. In particular, the straight line is extended in one of three directions: $-45°$, $0°$, $45°$ relative to the direction of the end point. However, if the distance is larger than $\tau_D/2$, the end points are left unconnected. The resulting image is denoted by $F(x, y)$.

3. EXPERIMENTAL RESULTS

The results of applying the proposed technique to two data sets with representative images shown in Figures 4a and 4g, respectively, are given here. The first set of images (*WSM*) was comprised of 512 images each 512×512 pixels in size, while the second set (*Lectin*) consisted of 821 images each 640×640 pixels.

As previously indicated the structures of interest reside mostly in the red components shown in Figures 4b and 4h, respectively. These were then thresholded as depicted in Figures 4c and 4j, respectively. In this case the window W used for the first data set was 16×16 pixels in size, whereas it was 20×20 for the second set. In addition, the value of R used was the maximum empirical variance and ensured that $\frac{s(x,y)}{R} \leq 1$. Finally, the value of the parameter k was empirically determined to be -0.1. Table 1 lists the various parameters used and their corresponding values. Note that different values are used for different dataset. Again, the values used were empirically determined.

Downloaded From: http://proceedings.spiedigitallibrary.org/ on 02/16/2017 Terms of Use: http://spiedigitallibrary.org/ss/termsofuse.aspx

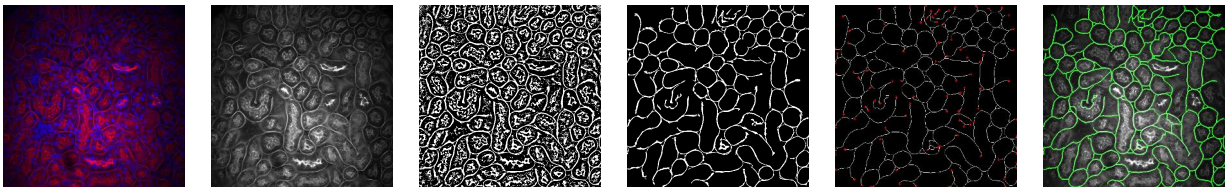

(a) Input image $I(x, y)$ (b) Red component $I_R(x, y)$ (c) $B(x, y)$ (d) $\tilde{B}(x, y)$ (e) $F(x, y)$ (f) $F(x, y)$ overlaid onto $I_R(x, y)$

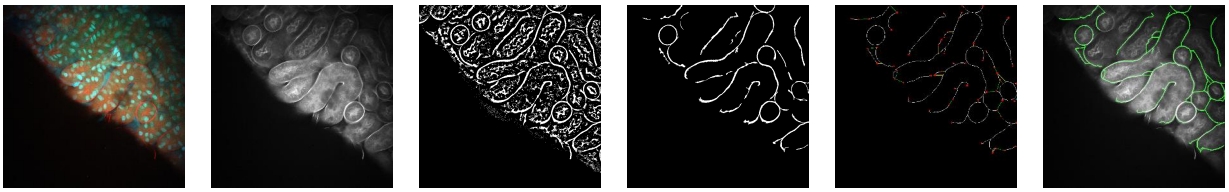

(g) Input image $I(x, y)$ (h) Red component $I_R(x, y)$ (i) $B(x, y)$ (j) $\tilde{B}(x, y)$ (k) $F(x, y)$ (l) $F(x, y)$ overlaid onto $I_R(x, y)$

Figure 4. Results of applying the proposed technique to the 81st image of the first data set, *WSM* (Top), and the 101st image of the second data set, *Lectin* (Bottom).

Parameters	Description	*WSM*	*Lectin*
k	Sauvola's parameter	-0.1	-0.1
T_G	Global threshold used to modify the local threshold	0	15
λ_1	Coefficient corresponding to P_P	0.25	0.25
λ_2	Coefficient corresponding to P_O	0.75	0.75
T_P	Threshold used for the total potential P_T and z direction refinement	0.8	0.8
σ_z	Standard deviation used for z direction refinement	0.5	0.5
τ_D	Matched end points distance threshold	35	40

Table 1. Parameters used in our proposed scheme.

As described above, the interiors were cleared out using connected component labeling and the boundaries pruned of any protruding branches. The outcome of these two steps is depicted in Figures 4d and 4j, respectively. Subsequently, the boundaries were closed. In Figures 4e and 4k red dots delineate the locations of all the end points, cyan curves indicate boundaries that were closed using ellipse fitting based on constrained least squares, green curves highlight the connection between two end points that do not belong to the same connected component, and the yellow straight lines are the extensions from non-matched end points to the closest boundary. The final boundaries are overlaid onto the original images as shown in Figures 4f and 4l, respectively.

In Figure 5, we compare the results of the proposed scheme to the 2D region-based active contour technique described in [7], when applied to images at various depths. The first and third rows exhibit the results of proposed scheme whereas the second and the fourth rows show the corresponding results using [7]. The 2D region-based active contour technique [7] needed 1000 iterations to converge to a solution as well as multiple circles to be used as initial contours. Furthermore, compared to the proposed technique, it did not capture as many boundaries of the various tubules. In particular, we observe that it successfully groups brighter regions in the images into one large object, but fails to delineate smaller objects or any objects for that matter in the darker regions.

4. CONCLUSION AND FUTURE WORK

This paper describes an algorithm that segments tubular structures in microscopy images based on adaptive and global thresholding, potentials, z direction refinement, branch pruning, end point matching, and boundary fitting. Compared to a region-based active contour technique, the proposed scheme was more successful at segmenting tubular structure in microscopy images. Future work will include extending this method to use region merging to combine small regions, utilizing additional shape information to aid in the separation of tubular structures that were joined together during the segmentation process, and extending the current technique to 3D.

Downloaded From: http://proceedings.spiedigitallibrary.org/ on 02/16/2017 Terms of Use: http://spiedigitallibrary.org/ss/termsofuse.aspx

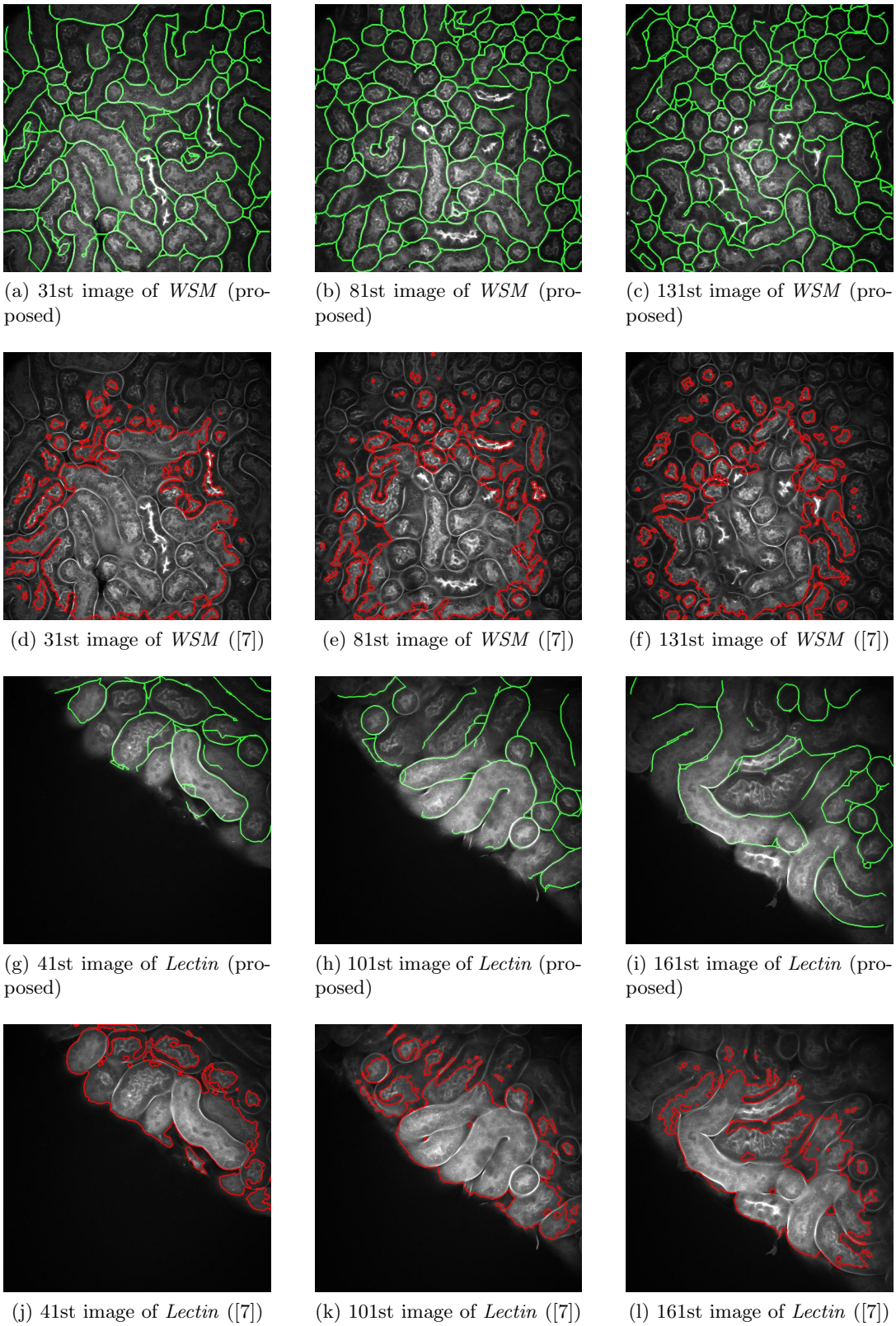

(a) 31st image of *WSM* (proposed)
(b) 81st image of *WSM* (proposed)
(c) 131st image of *WSM* (proposed)
(d) 31st image of *WSM* ([7])
(e) 81st image of *WSM* ([7])
(f) 131st image of *WSM* ([7])
(g) 41st image of *Lectin* (proposed)
(h) 101st image of *Lectin* (proposed)
(i) 161st image of *Lectin* (proposed)
(j) 41st image of *Lectin* ([7])
(k) 101st image of *Lectin* ([7])
(l) 161st image of *Lectin* ([7])

Figure 5. Comparison with 2D active contour at various depth.

Downloaded From: http://proceedings.spiedigitallibrary.org/ on 02/16/2017 Terms of Use: http://spiedigitallibrary.org/ss/termsofuse.aspx

Finally, the authors would like to thank Malgorzata Kamocka for acquiring and providing the data sets used in this work.

REFERENCES

[1] R. K. P. Benninger, M. Hao, and D. W. Piston, "Multi-photon excitation imaging of dynamic processes in living cells and tissues," *Reviews of Physiology Biochemistry and Pharmacology*, vol. 160, pp. 71–92, 2008.

[2] D. W. Piston, "Imaging living cells and tissues by two-photon excitation microscopy," *Trends in Cell Biology*, vol. 9, no. 2, pp. 66–69, 1999.

[3] P. T. C. So, C. Y. Dong, B. R. Masters, and K. M. Berland, "Two-photon excitation fluorescence microscopy," *Annual Review of Biomedical Engineering*, vol. 2, no. 1, pp. 399–429, 2000.

[4] J. A. Rosado-Toro and J. J. Rodriguez, "Cell splitting using dynamic programming," *Proceedings of the IEEE Southwest Symposium on Image Analysis and Interpretation*, pp. 33–36, April 2012, Santa Fe, NM.

[5] C. L. Phillips, L. J. Arend, A. J. Filson, D. J. Kojetin, J. L. Clendenon, S. Fang, and K. W. Dunn, "Three-dimensional imaging of embryonic mouse kidney by two-photon microscopy," *The American Journal of Pathology*, vol. 158, no. 1, pp. 49–55, January 2001.

[6] L. Vincent and P. Soille, "Watershed in digital spaces: an efficient algorithm based on immersion simulations," *IEEE Transactions on Pattern Analysis and Machine Intelligence*, vol. 13, no. 6, pp. 583–598, June 1991.

[7] T. F. Chan and L. A. Vese, "Active contours without edges," *IEEE Transactions on Image Processing*, vol. 10, no. 2, pp. 266–277, February 2001.

[8] G. Li, T. Liu, A. Tarokh, J. Nie, L. Guo, A. Mara, S. Holley, and S. T. C. Wong, "3D cell nuclei segmentation based on gradient flow tracking," *BMC Cell Biology*, vol. 8, no. 1, pp. 40, September 2007.

[9] X. Chen, X. Zhou, and S. T. C. Wong, "Automated segmentation, classification, and tracking of cancer cell nuclei in time-lapse microscopy," *IEEE Transactions on Biomedical Engineering*, vol. 53, no. 4, pp. 762–766, April 2006.

[10] A. Krtolica, C. O. Solorzano, S. Lockett, and J. Campisi, "Quantification of epithelial cells in coculture with fibroblasts by fluorescence image analysis," *Cytometry*, vol. 49, pp. 73–82, October 2002.

[11] B. Li and S. T. Acton, "Automatic active model initialization via poisson inverse gradient," *IEEE Transactions on Image Processing*, vol. 17, no. 8, pp. 1406–1420, August 2008.

[12] Y. He, N. Khanna, C. J. Boushey, and E. J. Delp, "Snakes assisted food image segmentation," *Proceedings of the IEEE International Workshop on Multimedia Signal Processing*, pp. 181–185, September 2012, Banff, Canada.

[13] G. Srinivasa, M. C. Fickus, Y. Guo, A. D. Linstedt, and J. Kovacevic, "Active mask segmentation of fluorescence microscope images," *IEEE Transactions on Image Processing*, vol. 18, no. 8, pp. 1817–1829, August 2009.

[14] K. S. Lorenz, P. Salama, K. W. Dunn, and E. J. Delp, "Three dimensional segmentation of fluorescence microscopy images using active surfaces," *Proceedings of the IEEE International Conference on Image Processing*, pp. 1153–1157, September 2013, Melbourne, Australia.

[15] A. Fakhrzadeh, E. Sporndly-Nees, L. Holm, and C. L. Luengo Hendriks, "Analyzing tubular tissue in histopathological thin sections," *Proceedings of the IEEE International Conference on Digital Image Computing Techniques and Applications*, pp. 1–6, December 2012, Fremantle, WA.

[16] H. Li and A. Yezzi, "Vessels as 4-D curves: Global minimal 4-D paths to extract 3-D tubular surfaces and centerlines," *IEEE Transactions on Medical Imaging*, vol. 26, no. 9, pp. 1213–1223, September 2007.

[17] F. Benmansour and L. D. Cohen, "Tubular structure segmentation based on minimal path method and anisotropic enhancement," *International Journal of Computer Vision*, vol. 92, no. 2, pp. 192–210, March 2010.

[18] L. M. Lorigo, O. Faugeras, W. E. L. Grimson, R. Keriven, R. Kikinis, A. Nabavi, and C.-F. Westin, "Codimension-two geodesic active contours for the segmentation of tubular structures," *Proceedings of the IEEE Conference on Computer Vision and Pattern Recognition*, vol. 1, pp. 444–451, June 2000, Hilton Head Island, SC.

Downloaded From: http://proceedings.spiedigitallibrary.org/ on 02/16/2017 Terms of Use: http://spiedigitallibrary.org/ss/termsofuse.aspx

[19] J. Sauvola and M. Pietikainen, "Adaptive document image binarization," *Pattern Recognition*, vol. 33, pp. 225–236, 2000.

[20] J. Canny, "A computational approach to edge detection," *IEEE Transactions on Pattern Analysis and Machine Intelligence*, vol. 8, no. 6, pp. 679–698, November 1986.

[21] L. Lam, S.-W. Lee, and C. Y. Suen, "Thinning methodologies-a comprehensive survey," *IEEE Transactions on Pattern Analysis and Machine Intelligence*, vol. 14, no. 9, pp. 869–885, September 1992.

[22] C. Lantuejoul and F. Maisonneuve, "Geodesic methods in quantitative image analysis," *Pattern Recognition*, vol. 17, no. 2, pp. 177–187, 1984.

[23] A. Fitzgibbon, M. Pilu, and R. B. Fisher, "Direct least square fitting of ellipses," *IEEE Transactions on Pattern Analysis and Machine Intelligence*, vol. 21, no. 5, pp. 476–480, May 1999.

Downloaded From: http://proceedings.spiedigitallibrary.org/ on 02/16/2017 Terms of Use: http://spiedigitallibrary.org/ss/termsofuse.aspx